JOURNAL OF MAGNETIC RESONANCE IMAGING 31:430–439 (2010)

Original Research

Topography Mapping of Whole Body Adipose Tissue Using A Fully Automated and Standardized Procedure

Christian Würslin, Dipl-Ing,[1,2*] Jürgen Machann, Dipl-Phys,[1] Hansjörg Rempp, MD,[1] Claus Claussen, MD,[3] Bin Yang, PhD,[2] and Fritz Schick, MD, PhD[1]

Purpose: To obtain quantitative measures of human body fat compartments from whole body MR datasets for the risk estimation in subjects prone to metabolic diseases without the need of any user interaction or expert knowledge.

Materials and Methods: Sets of axial T1-weighted spin-echo images of the whole body were acquired. The images were segmented using a modified fuzzy c-means algorithm. A separation of the body into anatomic regions along the body axis was performed to define regions with visceral adipose tissue present, and to standardize the results. In abdominal image slices, the adipose tissue compartments were divided into subcutaneous and visceral compartments using an extended snake algorithm. The slice-wise areas of different tissues were plotted along the slice position to obtain topographic fat tissue distributions.

Results: Results from automatic segmentation were compared with manual segmentation. Relatively low mean deviations were obtained for the class of total tissue (4.48%) and visceral adipose tissue (3.26%). The deviation of total adipose tissue was slightly higher (8.71%).

Conclusion: The proposed algorithm enables the reliable and completely automatic creation of adipose tissue distribution profiles of the whole body from multislice MR datasets, reducing whole examination and analysis time to less than half an hour.

Key Words: adipose tissue profiling; visceral adipose tissue; automatic image segmentation; metabolism; whole body MRI

J. Magn. Reson. Imaging 2010; 31:430–439.

OBESITY AND OVERWEIGHT are the emerging health problems of the past decades, not only in the Western world, but on a worldwide scale (1,2). However, not only the amount of total adipose tissue (TAT), but also its distribution and composition is of special importance in the pathogenesis of the concomitant diseases such as metabolic syndrome, type II diabetes, or coronary heart disease (3–7). Especially the two chemically almost identical, but morphologically and functionally different types of subcutaneous adipose tissue (SCAT) and visceral adipose tissue (VAT) have been reported to be of special interest (8,9). Furthermore, a strong correlation between the amount of adipose tissue (AT) in the neck and insulin resistance has been shown (10). Thus, methods for fast and accurate quantification of different AT compartments are desirable to improve the prediction of the risk for the occurrence of related diseases or to monitor lifestyle interventions.

Common techniques for quantification of body fat mass as body impedance analysis or underwater weighing (11) only provide information about the total amount of AT. Other anthropometric methods for the quantitative assessment of local fat, such as measurement of skin-fold thickness, waist circumference or waist-to-hip ratio, provide a simple and useful estimation of the proportion of abdominal fat, but are also unable to precisely distinguish between VAT and SCAT (12). MRI enables a reliable quantification of whole body AT as well as the distinction of different compartments (13,14).

A standardized whole body AT assessment procedure, which is able to show the distribution of all relevant AT compartments as well as the amount of total tissue (TT) in the body, has been proposed (15). However, the manual segmentation of these images is time consuming and requires the attention of an expert.

[1]Section on Experimental Radiology, Department of Diagnostic and Interventional Radiology, University of Tübingen, Tübingen, Germany.
[2]Chair of System Theory and Signal Processing, University of Stuttgart, Stuttgart, Germany.
[3]Department of Diagnostic and Interventional Radiology, University of Tübingen, Tübingen, Germany.
*Address reprint requests to: C.W., Section on Experimental Radiology, Department of Diagnostic and Interventional Radiology, Hoppe-Seyler-Str. 3, 72076 Tübingen, Germany.
E-mail: christian.wuerslin@med.uni-tuebingen.de
Received July 21, 2009; Accepted October 30, 2009.
DOI 10.1002/jmri.22036
Published online in Wiley InterScience (www.interscience.wiley.com).

Thus, it is desirable to automate this task. Methods for automatic quantification of abdominal AT distributions, distinguishing SCAT and VAT, have been described (16–18). However, none of these approaches is suited for evaluation of image slices of the whole body. A novel procedure, dividing the body into anatomic regions and creating standardized tissue profiles in each one of them, is proposed in this study.

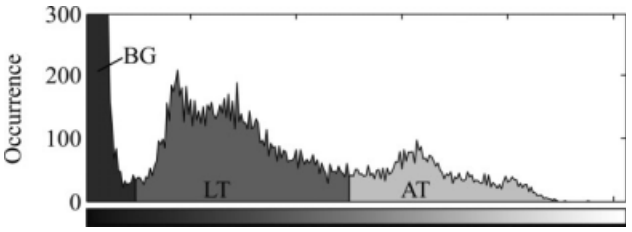

Figure 1. Typical histogram of a T1-weighted image and suggested division into three brightness classes.

MATERIALS AND METHODS

MR Data Acquisition

According to Machann et al (15), the images were acquired on a clinical 1.5 Tesla (T) whole body scanner (Magnetom Sonata, Siemens Medical Solutions, Erlangen, Germany). During examination, the volunteers were in the prone position with arms extended. A T1-weighted fast spin echo technique with an echo train length of 7 was applied, using $T_E = 12$ ms, $T_R = 490$ ms, slice thickness 10 mm, 5 slices per sequence, and 10-mm gap between slices. Field of view was 450 mm to 530 mm, depending on the volunteer's extension. Images with a 256 × 178 matrix were recorded, resulting in a voxel size of approximately 2 mm × 2 mm × 10 mm. Measuring time per sequence was 12 s, allowing breathhold examinations in abdominal and thorax regions. Data were collected from fingers to toes using the scanner's receive/transmit body coil. The given slice thickness and slice spacing resulted in 100 to 130 axial image slices per subject, depending on the volunteer's height. Total examination time was 20 min to 25 min.

The application of a standard fast spin echo sequence on the one hand enables a wide spread use of the proposed procedure, because this type of sequence should be available on any MR system. On the other hand, the SE technique allows compensation for inhomogeneities in the B_0 field without the need of any field shimming before image acquisition. Because the amount of TT is also subject to the evaluation procedure, a fat-only excited sequence was not used.

Fuzzy Clustering

Typical gray value histograms of T1-weighted MR images show three maxima. These correspond to the three prevailing classes background (BG) at the lower end of signal intensity, lean tissue (LT), having intermediate intensities and AT, having high intensity values (see Fig. 1). The notches in between these maxima are not empty, but populated with image elements with an intermediate intensity. These intensities are on the one hand caused by intensity nonuniformities (due to spatial coil characteristics and inhomogeneities of B_0 and B_1) and on the other hand by partial volume effects. The effects of an inhomogeneous B_0 field could be reduced by using a spin echo sequence, however, partial volume effects are particularly strong when using a low spatial resolution as in this case.

The first step in segmenting the acquired images into the desired compartments is to distinguish between these three classes by dividing the image histogram into three regions (see Fig. 1). It has been shown, that the so-called fuzzy c-means (FCM) algorithm delivers good results when segmenting MR images according to brightness (19,20). Considering an image function $I(x, y)$, assigning a scalar gray value (brightness) to each image coordinate $(x, y)^T$, the cost function of the FCM algorithm is given by:

$$J_{FCM} = \sum_x \sum_y \sum_{k=1}^{C} P_k^m(x,y)(I(x,y) - v_k)^2. \quad [1]$$

In this context, C is the number of clusters to be used, $P_k(x, y)$ is the probability of the pixel at position $(x, y)^T$ to belong to cluster k ($k \in [1..C]$), v_k is the centroid of class k and m is the so-called fuzziness and controls the blending of the membership probabilities. In this implementation, we chose $C = 3$ (the three intensity classes mentioned above) and $m = 2$. The cost function J_{FCM} is roughly a measure for the amount of image elements, which are still assigned to the wrong class. Thus, it is desired to minimize J_{FCM} which is archived iteratively by recomputing the cluster centroids v_k and membership probabilities P_k alternately, using Eqs. [2] and [3].

$$P_k(x,y) = \frac{|I(x,y) - v_k|^{-2/(m-1)}}{\sum_{k=1}^{C} |I(x,y) - v_k|^{-2/(m-1)}} \quad [2]$$

$$v_k = \frac{\sum_x \sum_y [P_k(x,y)]^m I(x,y)}{\sum_x \sum_y [P_k(x,y)]^m} \quad [3]$$

Although this fuzzy approach is widely used in the segmentation of MR images, the final results of P_k are usually used to create binary (hard) membership masks, by assigning each image element completely to the class k with the highest membership value P_k (maximum membership hard clustering). These hard masks will also be needed in some subsequent steps of the proposed algorithm and are denoted by M_1, M_2, and M_3. In the given application, however, the resolution of the axial image slices is relatively coarse and especially the slice thickness of 10 mm contributes to a high amount of partial volume effects. This applies especially to the transitions of AT and LT areas in abdominal areas. The proposed algorithm therefore uses the fuzzy membership values P_k for the creation of the final adipose tissue profiles. Thus, the fuzzy membership values are directly used as estimation for the

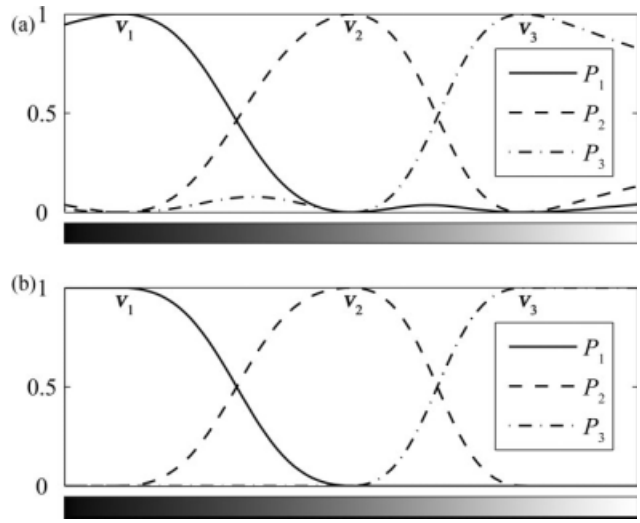

Figure 2. Class membership versus intensity after normal FCM algorithm (**a**) and after correction (**b**).

contribution of different tissue types to one image element. However, these fuzzy membership values need to be corrected with respect to two phenomena, which cause irrational results in the given application, which will be described in the following.

Assuming that an FCM algorithm with $C = 3$ converges, yielding cluster centroids $v_1 = 0.1$, $v_2 = 0.5$ and $v_3 = 0.8$ (brightness values normalized to fundamental range [0..1]), then Figure 2a shows the corresponding plots of the three membership probability functions P_1, P_2, and P_3 versus intensity. Due to the normalization term in the denominator of Eq. [2], the membership probabilities sum up to 1 for all intensity values. However, this causes, for example, the membership probability P_3 (AT class) of a very bright pixel ($I(x, y) > v_3$) to decrease again. The value of P_3 even decreases more, the higher the intensity $I(x, y)$ gets (see right end of the dashed-dotted line in Fig. 2a). This behavior is undesired in the given application, which is why all these irrational segments of P_1, P_2, and P_3 are corrected, resulting in the membership probabilities, shown in Figure 2b.

The second phenomenon is the direct transition from AT to BG areas. Image elements with partial volume effects are classified as LT by a standard FCM algorithm due to their intermediate brightness. These transitions are mostly found at the body contour, where SCAT areas and the surrounding air converge. Thus, the proposed algorithm corrects the regions near the body surface by setting $P_2 = 0$ before normalization of the probabilities. The result of this modified FCM clustering, applied to the image in Figure 3a can be seen in Figure 3b.

Body Division

To standardize the fat tissue profiles along the body axis, it is essential to accurately divide the body into

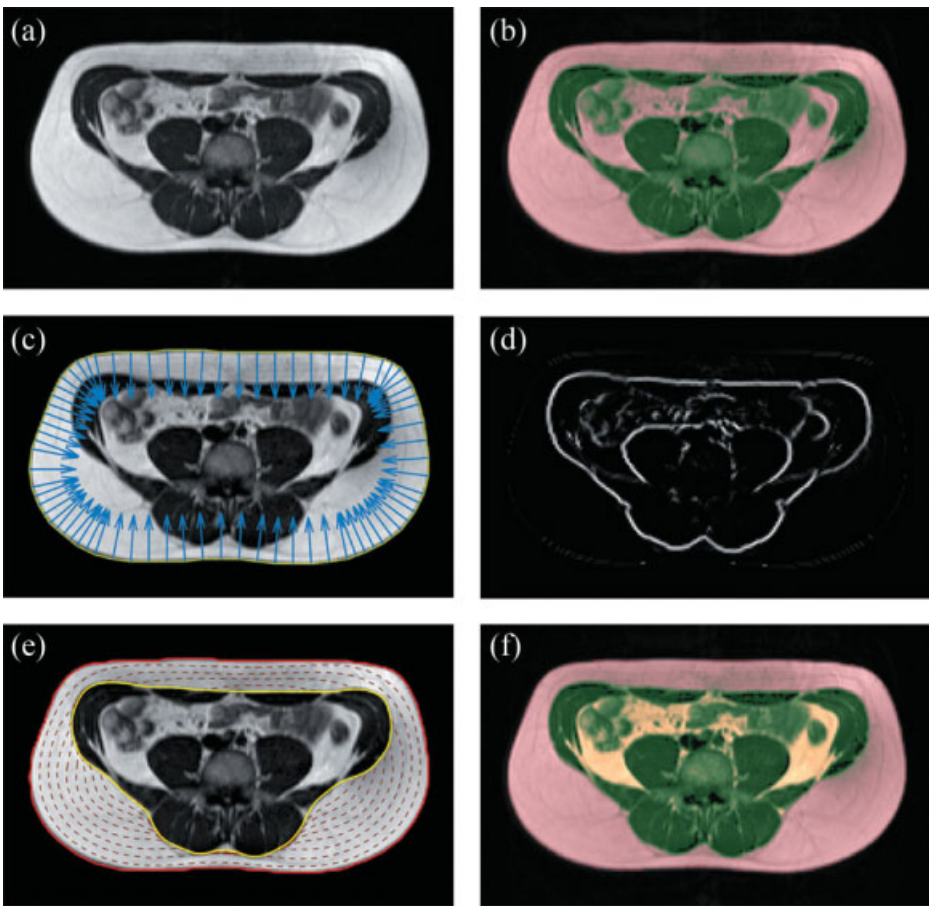

Figure 3. Demonstration of algorithm steps on abdominal image slice: original image (**a**), result of modified FCM algorithm (AT red, LT green, BG black; **b**), initial contour of snake algorithm and balloon forces (**c**), external energy field for snake algorithm (polar edge map; **d**), process of snake evolution from outer (red) to inner SCAT border (yellow; **e**), and final segmentation result (VAT yellow; **f**).

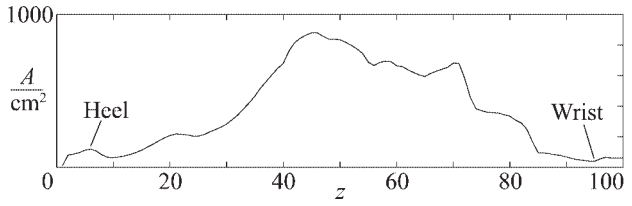

Figure 4. Preliminary total tissue (TT) profile and determination of wrist and heel positions.

anatomic regions. These regions are the lower extremities, trunk, and upper extremities (including the head). The boundaries of these regions are the shoulder and hip joints. Furthermore, for the standardization, the lower and upper borders of the body profiles are cropped to heels and wrists. The following sections explain how the whole MR dataset is divided into these anatomic regions and how the area, containing VAT was defined.

Detection of Wrist and Heel

To detect wrist and heel, a preliminary TT profile is used. This profile is obtained by plotting the slice-wise sum of P_2 and P_3 against the slice index z. The first local maximum as seen from the lower end of this TT profile is considered the image slice containing the heel. Similarly, the first local minimum as seen from the upper end is considered the wrist slice. An exemplary profile and the mentioned points are shown in Figure 4.

Detection of Head End

The end of the head is detected to get a good estimate of the volunteer's height. This estimation would be inaccurate if just detecting the wrist and heel, due to a varying bending of the elbow. The head end slice was defined as the first slice in the upper body half, no longer containing three but only two objects. The number of objects is obtained by considering all unconnected, black areas in M_1 as independent objects. Furthermore, all objects counting less than 200 pixels are disregarded. This step helps to find good estimates for the position of hip and shoulders, thus speeding up the subsequent step.

Detecting Hip and Shoulders

The hip- and shoulder-joints can be detected by parsing the images for the characteristic pattern, created by the heads of femur and humerus in axial images. In T1-weighted MR images, because of the high percentage of AT in the long bones of adults, they appear as two circular areas of a certain size and distance (see Fig. 5). Axial radii of caput humeri and caput femori and their distances were manually measured in 10 randomly chosen datasets (5 female, 5 male) to receive a valid target area. Mean values and standard deviation of these measures were calculated to $r = 20.8 \pm 2.2$ mm for the radii, $d_{CF} = 188.7 \pm 8.3$ mm for the distance between the caput femori and $d_{CH} = 295.8 \pm 15.8$ mm for the distance between the caput humeri.

Because of the assumption made above, the hard AT mask M_3 is parsed for circular areas. The circularity ρ of an object is calculated by considering the distance d of the object's border pixels to its centroid as a random variable and dividing the variable's mean value μ_d by its standard deviation σ_d:

$$\rho = \frac{\mu_d}{\sigma_d} \qquad [4]$$

For this application, a circularity threshold of 6.7 was empirically chosen to separate irregular from circular objects. Hip and shoulder slices are supposed to be detected, when two such circular objects are found with values for radii and distances not more than three times the standard deviation from the mean of the corresponding empirically determined values given above.

In cases where such circular objects are found in two adjacent slices (e.g., a joint has been cut twice) the slice with the greater radii is chosen to get the z-position nearest to the center of the joint. Due to the slice spacing of 10 mm and slice thickness of 10 mm, in a worst case scenario, the hip and shoulder joints will be found 10 mm away from their actual center.

Defining VAT Area

It is essential for the algorithm to know about the body regions in which inner AT compartments have to be separated and counted as VAT. Anatomically, this region was defined as the area reaching from the hip to the lower end of the heart. The lower end of this region is already well defined by the hip slice, obtained in the previous step. Due to the large amount of motion artifacts in the heart area, an automatic detection of the lower heart end was omitted. Instead, this upper margin of the VAT area is calculated, using an empirically determined index. This

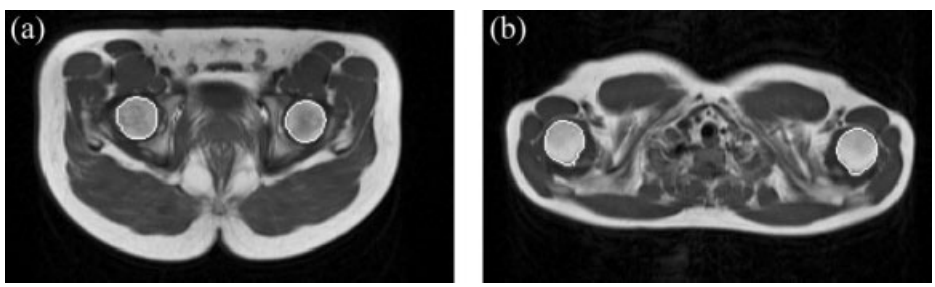

Figure 5. Image slices showing heads of femurs (**a**) and heads of humeri (**b**). The white lines indicate circular objects found by the algorithm.

index expresses the upper end of the VAT area as a fraction of the distance between the femoral head and the head of the humerus. This fraction was empirically determined to 0.66 from a cohort of 22 datasets ($\sigma = 0.04$).

Body Mask Creation

The purpose of this step is to separate the background from objects belonging to the body. As there are also signal-free areas inside the body (e.g., lungs), simply using the inverse of mask M_1 is not sufficient. However, M_1 is used as starting point for the creation of the body mask.

M_1 contains all pixels, with brightness close to zero, thus representing signal-free areas. To exclude signal-free areas inside the body from the body mask all, unconnected areas in M_1 which are not connected to the upper left corner of the image are deleted. The inversion of this mask contains all body objects and is referred to as the body mask in the following.

However, special care has to be taken in the thorax area, where images were usually corrupted by a considerable amount of motion artifacts, caused by the beating heart. To eliminate these small objects outside of the body, all objects with an area less than 400 pixels ($\asymp$16 cm^2) are deleted from the body mask. The situation is more complicated, if the misclassified artifacts are connected to the main body object. To get rid of these undesired extensions, a morphologic opening with a circular kernel with a radius of 20 pixels is applied to the body mask.

Dividing SCAT and VAT

To obtain the desired tissue profiles, the AT compartments found in the abdominal area have to be divided into the classes SCAT and VAT. Procedures to automatically separate these compartments have been proposed (16–18). In Liou et al (17), the separation is implemented using an elliptical fit of the inner SCAT contour and morphologic operations, while considering the anatomic properties of the different SCAT sections to get an accurate division of SCAT and VAT. In Kullberg et al (18), a gradient magnitude map is used in combination with an orthogonal convex hull tool and morphologic operations. The most versatile approach is presented in Positano et al (16), using so-called snakes, active contours which are able to lock onto image features such as edges, while obeying adjustable constraints to the contour shape. In the following, a two-staged version of this approach is presented, speeding up the separation procedure. It uses an extended snake algorithm with balloon forces (21), which is explained in the following.

Snake Algorithm

Snakes have first been introduced by Kaas et al (22), providing a tool to trace object contours even if subjective or discontinuous. These snakes, which can be considered a two-dimensional (2D) function $v(s) = (x(s), y(s))^T$ over a curve index s (or $v_i = (x_i, y_i)^T$, $i = [1 \ldots N]$ for the discrete case), iteratively adapt to image features by seeking a local minimum of the energy function:

$$E_{\text{snake}} = \int_0^1 E_{\text{int}}(\boldsymbol{v}(s)) + E_{\text{ext}}(\boldsymbol{v}(s))\, \mathrm{d}s. \qquad [5]$$

Here, E_{ext} is an external energy which can be derived from any image feature, such as edges or lines. The internal energy E_{int} provides smoothness constraints to the snakes by defining:

$$E_{\text{int}} = \frac{1}{2}\left(\alpha\left|\frac{\mathrm{d}\boldsymbol{v}(s)}{\mathrm{d}s}\right| + \beta\left|\frac{\mathrm{d}^2\boldsymbol{v}(s)}{\mathrm{d}s^2}\right|^2\right). \qquad [6]$$

The first term, weighted with parameter α makes the snake behave like a membrane, the second term, weighted with parameter β causes the snake to behave like a thin plate. By adjusting parameters α and β, the snake algorithm can be adapted to the given application.

To solve the minimization problem of E_{snake}, an iterative "evolution" of the snake is proposed by Kass et al. (22) by using the following equations:[1]

$$\begin{aligned} \boldsymbol{x}_{t+1} &= (\boldsymbol{A} + \gamma\boldsymbol{I})^{-1}(\gamma\boldsymbol{x}_t + \boldsymbol{f}_x(\mathbf{x}_t, \mathbf{y}_t)) \\ \boldsymbol{y}_{t+1} &= (\boldsymbol{A} + \gamma\boldsymbol{I})^{-1}(\gamma\boldsymbol{y}_t + \boldsymbol{f}_y(\mathbf{x}_t, \mathbf{y}_t)) \end{aligned} \qquad [7]$$

Here, vectors $\boldsymbol{x}$ and $\boldsymbol{y}$ (with iteration index t and $t + 1$, respectively) contain the x- and y- components of the i-th sampling point of a discrete snake contour $\boldsymbol{v}_i$. $\boldsymbol{A}$ is a pentadiagonal matrix containing functions of the internal energy parameters α and β, thus representing the snake's internal energy (see (22) for details) and $\boldsymbol{I}$ is the identity matrix. Parameter γ is a step size parameter. Vectors $\boldsymbol{f}_x$ and $\boldsymbol{f}_y$ contain the x- and y- components of the external energy for each snake point and are calculated as $f_x(i) = \partial E_{\text{ext}}/\partial x_i$ and $f_y(i) = \partial E_{\text{ext}}/\partial y_i$.

One major drawback of this method is that, unless the initial snake contour is chosen close to the desired contour (local minimum), the algorithm will either not find the desired contour or need a large number of iterations to find it. This is mostly due to the fact, that places far from the desired image features are likely to be force-free ($f_x, f_y \asymp 0$).

To overcome this problem one could use a smoothed version of the energy field E_{ext}, by applying a Gaussian lowpass. This, however, brings along the disadvantage of losing precise spatial information. A so-called Gradient Vector Flow (GVF) is introduced by Xu (23), which extends the snake's capture range significantly. However, the computation of the GVF is a minimization problem itself and computationally very expensive.

[1]The sign of f_x and f_y is negative in the original formulation in Kaas et al (22). The positive formulation in this study was chosen with respect to the usual representation of image edge maps, in which edges are represented by high (bright) values and snake points are supposed to be attracted by them.

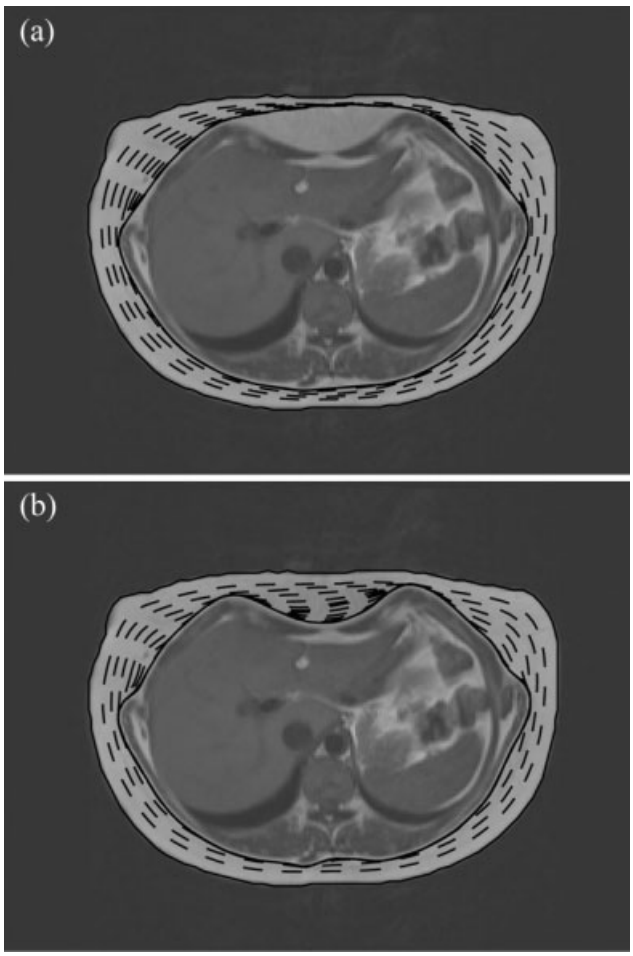

Figure 6. Comparison of evolution of a normal snake (**a**) and evolution of balloon snake (**b**).

If it can be granted that the snake is initialized on the outside of the desired contour, parameter α can be increased, which gives the snake the tendency of closing in even in areas free of external forces. However, increasing α also reduces the snake's ability of growing into concave structures, which can be seen in Figure 6a.

The idea of balloon snakes is the application of an additional force, pointing inward the closed contour for each contour point. This force is directed orthogonal to the contour's tangent vector at position i, in which the tangent vector $\boldsymbol{t}_i$ is approximated by the difference of the adjacent snake points $\boldsymbol{t}_i = \boldsymbol{v}_{i+1}\text{-}\boldsymbol{v}_{i-1}$. So the normalized orthogonal force at position i can be expressed by:

$$\boldsymbol{n}_i = \frac{1}{|\boldsymbol{t}_i|} \underbrace{\begin{pmatrix} 0 & 1 \\ -1 & 0 \end{pmatrix}}_{R} \boldsymbol{t}_i, \qquad [8]$$

where $\boldsymbol{R}$ is a matrix, rotating $\boldsymbol{t}_i$ by 90° and the factor $1/|\boldsymbol{t}_i|$ normalizes the force vector. The calculation of vector $\boldsymbol{n}_i$ is visualized in Figure 7. Finally, this force vector is considered when evolving the snake, by multiplying it with a weighting parameter ν and adding it to Eq. [7], resulting in

$$\begin{aligned} \boldsymbol{x}_{t+1} &= (\boldsymbol{A} + \gamma \boldsymbol{I})^{-1}(\gamma \boldsymbol{x}_t + \boldsymbol{f}_x(\boldsymbol{x}_t, \boldsymbol{y}_t) + \upsilon \boldsymbol{n}_x) \\ \boldsymbol{y}_{t+1} &= (\boldsymbol{A} + \gamma \boldsymbol{I})^{-1}(\gamma \boldsymbol{y}_t + \boldsymbol{f}_y(\boldsymbol{x}_t, \boldsymbol{y}_t) + \upsilon \boldsymbol{n}_y). \end{aligned} \qquad [9]$$

Here, $\boldsymbol{n}_x$ and $\boldsymbol{n}_y$ contain the x- and y- components of $\boldsymbol{n}$ for each snake point. Due to the additive nature and the easy calculation of $\boldsymbol{n}$, computation time is not significantly increased compared with the original snake approach. A comparison in the evolution of a conventional and a balloon snake algorithm is shown in Figure 6.

VAT Separation

As mentioned above, the balloon snake algorithm needs to be initialized outside the desired contour. This can be guaranteed by using the border of the body mask, obtained earlier. The first stage in the snake evolution is designed to quickly step over the bright SCAT ring and coarsely trace its the inner contour. It uses the balloon snake algorithm and relatively large values for the smoothness constraints α and β. The AT probability mask P_3 is used as external energy field E_{ext}. This causes homogeneous areas, such as the SCAT ring to be predominantly force-free. On the inner edge of the SCAT area, the transition from bright to dark intensity creates force vectors $\boldsymbol{f}_x$ and $\boldsymbol{f}_y$, pointing opposed to the orthonormal vectors $\boldsymbol{n}_x$ and $\boldsymbol{n}_y$, thus bringing the snake evolution to an end.

In the second step, an ordinary snake algorithm ($\nu = 0$) is used, this time with relatively small values of α and β, enabling the snake to accurately lock on to the edge, separating SCAT and inner tissues. Special care has been taken in choosing an external force for this evolution step. This time, the exact edge positions shall be found. To solve this problem, the image is usually filtered with an edge enhancement filter, such as a Laplacian filter, resulting in high intensity values at image edges and values close to zero in homogeneous areas. In this application, the desired edge is a bright-to-dark transition from the outside to the center of the image. Thus, it is desirable to only lock onto edges in this direction. A so-called polar edge map is used, containing only these edges, while canceling out

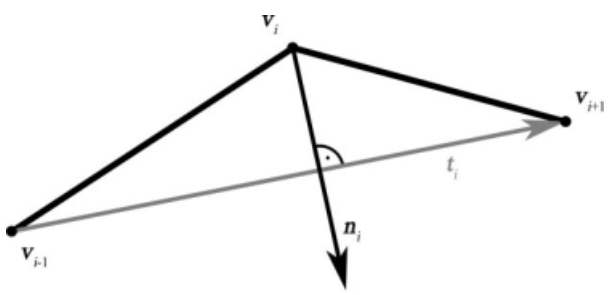

Figure 7. Computation of the additional balloon force in then balloon snake algorithm.

Table 1
Parameters of the Two-Stage Snake Algorithm

	α	β	γ	ν
1st step	0.25	0.5	0.7	0.2
2nd step	0.07	0.05	1	0

transitions in the opposite direction. This radial edge map can be computed, using:

$$E_{ext}(x,y) = \frac{1}{2}(|\nabla s(x,y)| + \boldsymbol{p}(x,y) \cdot \nabla s(x,y)) \qquad [10]$$

where $\boldsymbol{p}(x, y)$ is a vector, pointing away from the image center at all positions $(x, y)^T$ and $|\boldsymbol{p}(x, y)| = 1$. Edges, orthogonal to vector $\boldsymbol{p}(x, y)$ are still considered, but only have half the magnitude of radial bright-to-dark transitions, while image edges opposed to $\boldsymbol{p}(x, y)$ are canceled out.

The number of snake points used is determined by a desired minimum inter-point distance of the snake points. Whenever the distance between two adjacent snake points gets below this value (due to snake evolution) one of the points is removed. This value was chosen to one pixel (approximately 2 mm for the given field of view and image resolution), resulting in inter-point distances between 1 and 2 pixels. The complete list of values of the snake evolution parameters for both steps can be found in Table 1.

Quantifying SCAT of the Neck

Recently, a high correlation between the amount of SCAT in the neck and insulin sensitivity has been shown (10). As an estimation for the total amount of this AT compartment, the posterior SCAT in the shoulder slice, deliminated by the heads of the left and right humerus can be used. To divide SCAT from inner AT components, the same procedure as used to separate SCAT and VAT in the abdomen is used. The heads of the left and right humerus are detected in the body division step.

Bone Marrow

Bone marrow (BM) is not especially regarded in the proposed algorithm and included in the amount of total AT and VAT. In some applications this might not be desirable, because BM is functionally different from most other AT compartments. However, using the proposed algorithm, the class of VAT is usually not affected by BM because the BM in the trunk is quite dark and not detected as AT by the FCM algorithm. In the extremities, the bright BM is detected as AT and contributes to the amount of total AT. However, this behavior was not considered significant, because the amount of BM in the extremities is very similar for different volunteers and only scales slightly with the volunteer's height.

Profile Creation and Standardization

To obtain the desired tissue profiles, in each image slice the probabilities P_1, P_2 and P_3 are accumulated across all image coordinates $(x, y)^T$, multiplied by the in-plane pixel dimension and plotted against the slice index z. To standardize these profiles, they are piecewise linear interpolated in the three sections lower extremities (70 sampling points), trunk (50 sampling points), and upper extremities (40 sampling points).

Evaluation Procedure

For quantitative analysis of the suggested algorithm, the automatically obtained tissue profiles of 20 volunteers with body mass index (BMI) range 18.5 to 40.4 ($\mu = 28.4 \pm 7.1$ kg/m^2) were compared with manually obtained profiles. The manual profiles were obtained using a semiautomatic procedure consisting of thresholding the images at two different intensity levels (to separate BG, LT, and AT) and drawing regions of interest to separate SCAT and VAT in abdominal areas.

To evaluate the algorithm's repetition accuracy, three volunteers ($23.1 < \text{BMI} < 32.8$) were measured twice, the second time after repositioning and new adjustment of the scanner. The algorithm was performed on both datasets of the corresponding volunteers and the resulting standardized profiles compared.

For each dataset and tissue class, two figures were extracted. The first one is the mean over all image slices of the slice-wise absolute tissue area difference, expressed as percentage of the amount of manually obtained area of total tissue in that slice:

$$|\overline{\Delta A}| = \frac{1}{N}\sum_{z=1}^{N}\frac{|A_a(z) - A_m(z)|}{A_{TT,m}(z)}, \qquad [11]$$

where z is the slice index and N the number of image slices in one dataset (subscript index "TT" refers to tissue class, indices "m" and "a" to manual and automatic). This value can be considered a measure of the algorithm's absolute accuracy. The second figure is calculated in the same way as the first, except, that it uses simple differences rather than absolute ones. Thus it is calculated by:

$$\overline{\Delta A} = \frac{1}{N}\sum_{z=1}^{N}\frac{A_a(z) - A_m(z)}{A_{TT,m}(z)}. \qquad [12]$$

This value does not represent the algorithms accuracy because positive and negative values might cancel out each other. However, it is a good estimator of whether the algorithm tends to overestimate (positive values) or underestimate (negative values) a certain tissue class. In the repetition accuracy study, only the first one of these values was calculated because there was no gold standard.

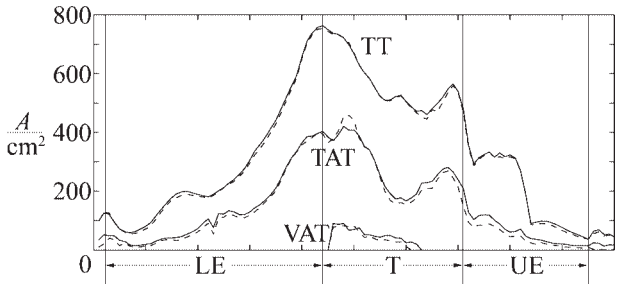

Figure 8. Comparison of manually (dashed lines) and automatically (solid lines) obtained tissue profiles. TT, total tissue; TAT, total adipose tissue; VAT, visceral adipose tissue.

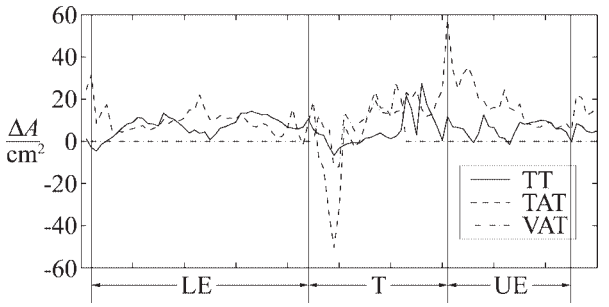

Figure 9. Difference between automatically and manually obtained tissue profiles in Figure 8 for classes total tissue (TT), total adipose tissue (TAT) and visceral adipose tissue (VAT).

RESULTS

The automatic segmentation algorithm was implemented on a standard mobile computer (Core 2 Duo, 2 GHz, 2 GB RAM) using MATLAB (The MathWorks, Inc). Total segmentation time was 76.1 ± 6.6 s per dataset (105 ± 5.5 image slices per dataset).

Structures, delimiting the anatomic regions according to section *Body Division* (heels, hip, shoulders, and wrists) were reliably detected in all volunteers, even if the subject was located slightly tilted in the scanner.

In 9 of 373 abdominal slices (2.41%), in which the VAT area was determined, the snake algorithm partly failed to detect the desired border. This occurred exclusively in very skinny volunteers, where the SCAT ring was very thin.

A plot, comparing the automatically and manually obtained tissue profiles of one volunteer is shown in Figure 8. The dashed lines correspond to the manually obtained profiles, solid lines to the automatically obtained profiles. In Figure 9, the differences between two corresponding lines (e.g., the difference between manually and automatically obtained profiles for each tissue class) are plotted for the same dataset.

In Figure 10a, the mean absolute difference values of all tissue classes and all 20 volunteers (calculated using equation 11) are shown are plotted against BMI. These values vary in between 2.62% and 9.41% for TT, 4.64% and 14.20% for total AT (TAT) and 1.18% and 7.13% for VAT. In Table 2, the average of these values are given for four different BMI classes (normal, overweight, obese I, and obese II/III).

Figure 10b, shows a plot very similar to Figure 10a. However, this time the mean difference values (calculated using equation 12) are shown. These values vary in between −1.12% and 8.77% for TT, 3.90% and 14.20% for TAT, and 1.13% and 7.13% for VAT. Table 3 shows the average of these values, again for four different BMI classes.

A comparison of the automatically and manually obtained areas of AT in the neck (shoulder slice) showed a good correlation, with a mean absolute difference of 4.20%, expressed as percentage of the manually obtained area.

By measuring three volunteers twice, a very good repetition accuracy could be proved. Especially the class of VAT showed a very low mean absolute deviation value between measurements of only 1.13%. The class of TT showed a mean absolute deviation of 3.08% and the class of TAT a mean absolute deviation of 1.48%. The deviation values for all three volunteers can be found in Table 4. An inspection of the tissue profiles of this repetition study showed, that the high deviation value of the TT class was mainly caused by the strong motion artifacts in the thorax area.

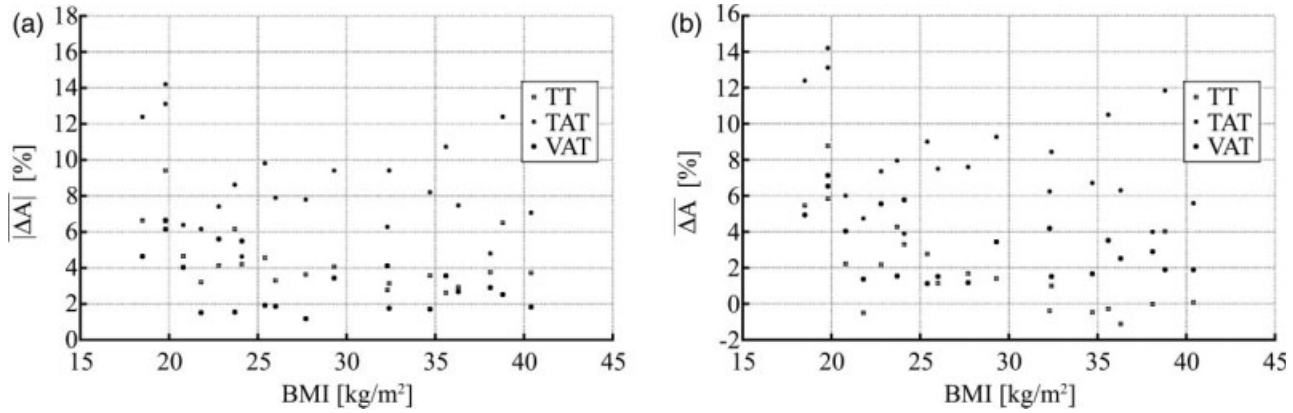

Figure 10. Values of mean absolute difference (**a**) and mean difference (**b**) of in-slice tissue area for classes total tissue (TT), total adipose tissue (TAT), and visceral adipose tissue (VAT) for all 20 datasets plotted versus BMI.

Table 2
Mean Values of In-slice Absolute Differences Between Manually and Automatically Obtained Tissue Areas for Different BMI Classes

BMI group [kg/m^2]	$\overline{\lvert\Delta A_{TT}\rvert}$ [%]	$\overline{\lvert\Delta A_{TAT}\rvert}$ [%]	$\overline{\lvert\Delta A_{VAT}\rvert}$ [%]
18–24.9	5.63	9.12	4.61
25–29.9	3.90	8.73	2.10
30–34.9	3.16	7.97	2.53
35–40.5	3.91	8.50	2.70
Overall	4.48	8.71	3.26

Table 3
Mean Values of In-slice Differences Between Manually and Automatically Obtained Tissue Areas for Different BMI Classes

BMI group [kg/m^2]	$\overline{\Delta A_{TT}}$ [%]	$\overline{\Delta A_{TAT}}$ [%]	$\overline{\Delta A_{VAT}}$ [%]
18–24.9	3.94	8.71	4.61
25–29.9	1.75	8.34	1.82
30–34.9	0.05	7.13	2.46
35–40.5	0.54	7.64	2.54
Overall	2.07	8.13	3.21

DISCUSSION

Due to the increasing world-wide occurrence of obesity and of the resulting complications, such as type II diabetes or coronary complications (1,2), methods for monitoring AT in the body are of increasing importance. In this, the total amount of AT without considering the location in the body seems to be less promising in the prediction of metabolic complications, than the precise distinction of specific compartments, such as SCAT, VAT, and AT in the neck and its spatial distribution (3–10). By using MRI, these compartments can be assessed and used to create standardized tissue profiles of the whole body, while avoiding the use of ionizing radiation (13–15). To reduce the time and personnel needed for the segmentation of appropriate MR datasets, this study proposes an integrated method for standardized and region-depended assessment of AT volumes.

The primary goal of the proposed algorithm is to work completely without any user interaction, creating the need of a robust routine. The most challenging step is the division of the body into anatomic regions, which succeeded for all volunteers in the study. Also, the separation of SCAT and VAT, using a modified snake algorithm achieved the desired results in 97.59% of all cases, which is also an indicator for the robustness of the method.

The automatically obtained TT profiles showed good correlation with those, obtained manually (overall mean absolute difference 4.48%). The TT profiles showed the strongest deviation in the thorax area, where images were heavily corrupted by motion artifacts caused by the heart. The mean absolute differences was significantly above average for the BMI class of normal weight persons (5.63%) and below average for the three remaining classes. The correlation between BMI and mean absolute differences was calculated to $r = -0.49$, indicating a tendency to higher deviation values for lower BMI values. The overall mean difference value of 2.07% shows that the algorithm tends to slightly overestimate the amount of TT. Again, this behavior was stronger for the class of normal weight volunteers, whereas for the two classes of obese volunteers, a tendency was hardly recognizable.

The TAT profiles showed a higher overall mean absolute difference of 8.7%. Here, the automatically obtained amount of TAT was usually higher in the extremities and significantly higher in feet and hands, as bone marrow was mainly considered as AT by the algorithm. However, due to the cropping to the area in between heels and wrists, feet and hands do not contribute to final, standardized profiles. The amount of TAT was usually obtained accurately in abdominal slices. However, motion artifacts in the thorax area made an accurate tissue profiling difficult. The correlation between BMI and mean absolute differences, as well as mean differences was very low, indicating a similar behavior for all BMI classes. Generally, the mean difference values were very close to those of the mean absolute differences, indicating the algorithm's tendency to overestimate the amount of TAT compared with manual segmentation for all BMI classes.

The VAT profiles showed a lower overall mean absolute difference than TAT (3.28%). Just like for TT, this value was above average for the class of normal weight volunteers (4.52%) and below average for all other classes. The values of the mean differences again show that the algorithm tends to overestimate the amount of VAT in a vast majority of cases (overall 3.21% overestimation).

A visual inspection of the segmented images showed that the overestimation of VAT in the class of normal weight volunteers was mainly caused by the lack of a significant amount of AT in the abdominal area. This causes the FCM-algorithm to detect the bone marrow of pelvis and spine (which is slightly brighter than surrounding LT, but usually detected as LT in obese volunteers) to be detected as VAT. In very lean subjects (BMI < 20), even parts of the liver were detected as VAT due to the lack of AT present.

The amount of AT in the neck, which has been shown to be an important and reliable indicator for

Table 4
Comparison of Automatically Obtained, Standardized In-slice Tissue Areas After Repositioning

Volunteer	BMI	$\overline{\lvert\Delta A_{TT}\rvert}$ [%]	$\overline{\lvert\Delta A_{TAT}\rvert}$ [%]	$\overline{\lvert\Delta A_{VAT}\rvert}$ [%]
1	23.1	2.51%	1.31%	1.35%
2	27.8	4.08%	1.70%	0.75%
3	32.8	2.66%	1.44%	1.29%
Overall		3.08%	1.48%	1.13%

the prediction of insulin resistance was quantified with a high accuracy.

In conclusion, this study proposes a robust, automatic segmentation method with a high repetition accuracy, supplying standardized whole body AT profiles and additional, meaningful measures for metabolism risk indication and intervention monitoring. The proposed algorithm is capable of reducing the total examination time to less than 30 min.

REFERENCES

1. World Health Organization. Obesity: preventing and managing the global epidemic. WHO Technical Report Series 894. Geneva: World Health Organization; 2000.
2. Hedley AA, Ogden CL, Johnson CL, Carroll MD, Curtin LR, Flegal KM. Prevalence of overweight and obesity among US children, adolescents and adults, 1999–2002. JAMA 2004;291:2847–2850.
3. Kissebah AH, Vydelingum N, Murray R, Evans DJ, Kalkhoff RK, Adams PW. Relation of body fat distribution to metabolic complications of obesity. J Clin Endocrinol Metab 1982;54:254–260.
4. Krotkiewski M, Björntorp P, Sjöström L, Smith U. Impact of obesity on metabolism in men and women. Importance of regional adipose tissue distribution. J Clin Invest 1983;72:1150–1162.
5. Ohlson LO, Larsson B, Svärdsudd K, et al. The influence of body fat distribution on the incidence of diabetes mellitus. 13.5 years of follow-up of the participants in the study of men born in 1913. Diabetes 1985;34:1055–1058.
6. Larsson B, Bengtsson C, Björntorp P, et al. Is abdominal body fat distribution a major explanation for the sex difference in the incidence of myocardial infarction? The study of men born in 1913 and the study of women, Göteborg, Sweden. Am J Epidemiol 1992;135:266–273.
7. Carr MC, Brunzell JD. Abdominal obesity and dyslipidemia in the metabolic syndrome: importance of type 2 diabetes and familial combined hyperlipidemia in coronary artery disease risk. J Clin Endocrinol Metab 2004;89:2601–2607.
8. Kahn BB, Flier JS. Obesity and insulin resistance. J Clin Invest 2000:106:473–481.
9. Wajchenberg BL. Subcutaneous and visceral adipose tissue: their relation to the metabolic syndrome. Endocr Rev 2000;21: 697–738.
10. Machann J, Oppek KD, Stefan N, et al. Quantification of subcutaneous adipose tissue of the neck and correlation to insulin sensitivity. MAGMA Suppl. (CD) 2008. DOI:10.1007/s10334–008-0123–5.
11. Brodie DA, Sewart AD. Body composition measurement: a hierarchy of methods. J Pediatr Endocrinol Metab 1999;12:801–816.
12. Chan DC, Watts GF, Barrett PH, Burke V. Waist circumference, waist-to-hip ratio and body mass index as predictors of adipose tissue compartments in men. Q J Med 2003;96:441–447.
13. Abate N, Burns D, Peshock RM, Garg A, Grundy SM. Estimation of adipose tissue mass by magnetic resonance imaging: validation against dissection in human cadavers. J Lipid Res 1994;35: 1490– 1496.
14. Shen W, Wang Z, Punyanita M, et al. Adipose tissue quantification by imaging methods: a proposed classification. Obes Res 2003;11:5–16.
15. Machann J, Thamer C, Schnoedt B, et al. Standardized assessment of whole body adipose tissue topography by MRI. J Magn Reson Imaging 2005;21:455–462.
16. Positano V, Gastaldelli A, Sironi AM, Santarelli MF, Lombardi M, Landini L. An accurate and robust method for unsupervised assessment of abdominal fat by MRI. J Magn Reson Imaging 2004;20:684–689.
17. Liou TH, Chan WP, Pan LC, Lin PW, Chou P, Chen CH. Fully automated large-scale assessment of visceral and subcutaneous abdominal adipose tissue by magnetic resonance imaging. Int J Obes (Lond) 2006;30:844–852.
18. Kullberg J, Ahlström H, Johansson L, Frimmel H. Automated and reproducible segmentation of visceral and subcutaneous adipose tissue from abdominal MRI. Int J Obes (Lond) 2007;31:1806–1817.
19. Bezdek JC, Hall LO, Clarke LP. Review of MR image segmentation techniques using pattern recognition. Med Phys 1993;20:1033–1048.
20. Hall LO, Bensaid AM, Clarke LP, Velthuizen RP, Silbiger MS, Bezdek JC. A comparison of neural network and fuzzy clustering techniques in segmenting magnetic resonance images of the brain. IEEE Trans Neural Netw 1992;3:672–682.
21. Cohen LD. On active contour models and balloons. CVGIP: Image Understanding 1991;53:211–218.
22. Kaas M, Witkin A, Terzopoulos D. Snakes: active contour models. Int J Comput Vision 1988;1:321–331.
23. Xu C, Prince JL. Snakes, shapes and gradient vector flow. IEEE Trans Image Process 1998;7:359–369.